UC Riverside
UC Riverside Previously Published Works

Title

Monitoring creep along the Hayward Fault using structure-from-motion photogrammetry of offset curbs

Permalink

Journal

ISSN

Authors

Swiatlowski, Jerlyn L
Funning, Gareth J
Barth, Nicolas C

Publication Date

DOI

Monitoring creep along the Hayward Fault using structure-from-motion photogrammetry of offset curbs

Jerlyn L. Swiatlowski, Gareth J. Funning, and Nicolas C. Barth

Department of Earth and Planetary Sciences, University of California, Riverside, CA 92521, USA

ABSTRACT

We present observations of sidewalk curbs that are offset by creep on the Hayward Fault in Fremont, California. Using structure-from-motion photogrammetry techniques, we construct 3D models from suites of 2D photos taken from 2015 to 2018 at 20 sites along the fault. By aligning and comparing these models, we measure the 3D displacements of each offset sidewalk through time at precisions of ~0.5 mm/yr. We find that on average individual offset curbs record <40% of the overall creep rate measured at nearby alignment arrays (which span a fault-perpendicular distance of 100 m or more). The 'fault trace' can more accurately be considered a zone of deformation, narrower than an alignment array width but wider than one curb length (~3-5 m). Sites for which we have multiple time intervals to compare show inter-annual temporal variability in creep rate and direction. Our methods offer a new, complementary approach to cheaply and efficiently document creep-related deformation in an urban setting, one that may be particularly useful for tracking deformation of engineered materials and their cohesion to the subsurface. Given the use of readily available equipment (consumer-grade camera, GPS, ruler), ease of data collection, and accessibility of urban field sites, we believe that this style of monitoring would lend itself particularly well to citizen science efforts.

Key words: Creep and deformation; Transient deformation; Image processing; Fractures, faults, and high strain deformation zones

INTRODUCTION

The Hayward Fault, in California's San Francisco Bay Area, has had twelve known surface-rupturing earthquakes in the last ~2000 years (Lienkaemper & Williams, 2007; Lienkaemper et al., 2010). The last known event was a ~M6.9 earthquake in 1868 with a mean slip of 1.9 ± 0.4 m (Yu & Segall, 1996) and an estimated rupture length of 45–60 km, approximately from Berkeley to Fremont (Lienkaemper & Galehouse, 1998). While there have been no surface-rupturing earthquakes on the Hayward Fault in the time since, surface offsets along the fault trace due to aseismic creep are ongoing. From a seismic hazard standpoint, the occurrence of creep results in reduced strain accumulation on a fault, and possibly also a reduced ability to sustain seismic rupture (e.g. Field et al., 2013; Lozos et al., 2015). As a result, to correctly assess future seismic hazard, there have been many studies documenting the creep rate along the entire fault length, including near-field measurements made using creepmeters and alignment arrays (e.g., Bilham et al., 2009; Lienkaemper et al., 2014; McFarland et al., 2016, 2019) and models constrained using space geodetic techniques such as GPS and InSAR (e.g., Schmidt et al., 2005; Burgmann et al., 2000). The rate of fault creep varies along the fault from ~2.6 mm/yr to ~7.9 mm/yr, with the highest creep rates located at the southeastern end of the fault, in the city of Fremont (Lienkaemper et al., 2014, Figure 1).

While the presence of creep on the fault may reduce the amount of seismic moment that could be released in future earthquakes, it can still pose a threat in the short term to fault-crossing infrastructure. In Fremont and the other cities that lie along the fault, fault creep can cause ongoing damage to human-built infrastructure such as fences, buildings, pipes, roads, and sidewalks. Cities undertake constant repairs of such infrastructure for the safety of the citizens, including realignment of curbs (e.g., Lin, 2016), and buildings built across the fault that have been deemed unsafe due to infrastructure flaws. Prominent examples of abandonment include Hayward's City Hall built in the 1930s (Stoffer, 2008) and the University of California, Berkeley's Memorial Stadium (Radbruch & Lennert, 1966; Doolin et al., 2005). An improved understanding

of the rates and distribution of fault creep can also benefit infrastructure projects in terms of planning for and mitigating damage from ongoing surface slip.

In this study, we monitor fault creep from offset cultural features within the city of Fremont, CA (population: 236,000), where the Hayward Fault's creep rate is highest. We focus on curb offsets where streets intersect with mapped traces of the fault as these are readily accessible and can progressively record deformation. The offset curbs allow us (1) to document how the urban environment accommodates fault creep, and (2) to better define the width of the deformation zone being expressed in the urban setting along the creeping Hayward Fault.

We measure 21 curb sites, selected from 36 monitored from 2009 to 2011 (e.g. Funning et al., 2010; Figure 1, Table S1, S2). Funning et al. (2010) used an inexpensive point-and-shoot digital camera on a tripod 1.0 meter above the curb offset, leveled to the horizontal, and centered on the offset, such that horizontal displacement of the curb could be identified by aligning and comparing static photographs from different dates. Two photos were taken; one with a compass, handheld GPS, and tape measure in frame, and one without. In multiple cases, increasing offsets could be detected from comparisons of these photos, and verified against manual measurements of the offset curbs with a ruler.

In our study, we apply the structure-from-motion (SfM) photogrammetry technique to monitor the 3D displacement field of curbs from 2015 to 2018. SfM can render the 3D structure of an object from multiple overlapping photographs taken from different vantages around the object in question. SfM is not a new method, but improvements in computing power and development of computationally efficient and user-friendly software has made its applications to geoscience widespread and effective in recent years (e.g. Westoby et al., 2012). Using SfM eliminates the need to carefully align and level the camera in the field, allowing for rapid data collection by a novice photographer, and enables the full 3D form to be captured as a 'point cloud' of identified points on the surface of the survey target.

In recent years, analysis using the iterative closest point (ICP) algorithm, which finds the solid body transformation necessary to align two point clouds, or subsets of those point clouds, has

been used on data sets acquired at different times to detect the surface displacement that occurred between point cloud acquisitions. This approach has successfully detected spatially varying three-dimensional surface displacements due to landsliding (e.g. Teza et al., 2007), coseismic deformation (e.g. Nissen et al., 2014) and fault creep on the San Andreas Fault (Scott et al., 2020a). Although early studies focused on point clouds obtained from lidar surveys, similar ICP-based approaches have recently been used successfully on SfM-derived point clouds (e.g. Scott et al., 2020b). Here we apply SfM to generate detailed 3D point clouds of a series of curbs spanning the active trace of the Hayward fault from different years, then align them using the ICP algorithm to estimate the 3D displacement of each offset curb, and ultimately estimate the surface manifestation of shallow creep.

METHODS

Field Acquisition

We used a digital camera with a fixed focal length lens to take photographs of curbs every year from 2015 to 2018. In some cases, some sites were not photographed on every visit due to accessibility issues, such as obstruction by parked cars. Photos were taken during all weather conditions, but we found that the most useful photographs were taken under overcast skies that provided even lighting with minimal shadowing (a canopy could also be used to minimize shadows). Prior to photographing, we cleared each site of debris and vegetation and positioned a note card with the site number, a compass, and a 5 cm wooden cube used for scale next to the curb offset. Overlapping photographs were taken within ~2 meters of the offset feature at multiple high and low vantage points to document the offset curb from a wide array of inward-looking positions.

We found painted curbs (e.g., from fire lanes or disabled parking zones) to be problematic because the paint can obscure distinguishing features (such as cracks or gravel clasts in concrete), are frequently repainted, and the thickness of the paint over time can become a source of error

when trying to measure mm–scale differences in the sidewalks with larger time intervals. Though we did not use them, including multiple (at least four) permanently implanted physical reference markers at each site (e.g. survey pins, concrete nails) at important sites would allow for fast and accurate alignment.

Structure-from-Motion Multi-View Stereo (SfM-MVS) Processing

SfM is an image-based modeling method which attempts to recover camera parameters, orientation, and the camera position (i.e., where the camera was when the photo was taken) from a set of overlapping 2D photos to infer the 3D scene structure from a set of differently oriented photos of a target (e.g. James and Robson, 2012; Westoby et al., 2012; Fonstad et al., 2013). We use the Agisoft Metashape Pro software package, which uses the SIFT algorithm (Lowe, 1999) to solve for camera positions and build a sparse 3D point cloud of all feature points that represents the main structure of the object within a local, relative coordinate system (e.g. Bemis et al., 2014). The multi-view stereo (MVS) method is then used to construct a dense point cloud (9,000,000 points in the dense cloud from 20,000 points in the sparse cloud is typical for our models). The final product is in a relative coordinate system suitable for our purposes. We used the wooden cube's position and dimensions as the necessary ground control points and scale to define a local X, Y, Z coordinate system. Model uncertainties are greatest at the periphery of the model due to fewer overlapping photographs observing the 'far field'; we account for the possibility of unrealistic 'warping' by excluding these areas from our analysis.

Alignment of Point Clouds to Measure Curb Movement

To determine the relative displacement between models due to fault creep, we export dense point clouds for the same site on two different acquisition dates from Metashape as LAS files and align them in the CloudCompare software (cloudcompare.org). Our convention is to align the point cloud on the left side of the curb offset, from a vantage point that faces the curb wall from the road, with the goal of measuring the displacement between the point clouds on the other

(right) side of the offset. There are two steps to aligning data from the same curb from two different dates; first, a manual rough alignment, followed by fine alignment using the Iterative Closest Point (ICP) method (Chen & Medioni, 1992). For the rough alignment we manually pick anchor points that are visually identifiable (by both color and texture) in both point clouds on the left side of the curb offset. We choose at least six anchor points in the horizontal plane and at least two points in the vertical plane. The distribution of anchors needs to cover a wide enough area that the point cloud aligns both close to and far from the offset. An example of a candidate anchor is the corner of a gravel clast within the cement of the sidewalk and/or curb (Figure S1). The rough alignment will translate and rotate one point cloud into the other to find the best fit to all anchors.

Once the rough alignment is complete, features that have the potential to be different between photo acquisition dates are removed. These include vegetation, tooled control joint gaps between curb segments, the note card with the site number, and the reference scale. We also narrow the focus of the point cloud and cut out everything more than ~2 meters from the offset on each side, to minimize the influence of possible far field artifacts on our analysis.

We then carry out a fine alignment using the ICP algorithm, which aligns two irregular point clouds by minimizing the distance between point-pair distances with an iterative rigid body transformation consisting of a translation and rotation. This process repeats, minimizing the mean square error between all paired points until a global minimum is met (e.g. Nissen et al., 2012).

We next use the ICP method to align points on only one side of the offset; we first subdivide the left and right side of the curb offset as two distinct point clouds, then apply the ICP method to finely align the left-side points only. This is necessary to account for the different local reference frames of the two different point clouds. We then take the rigid body transformation matrix used to finely align the left-side points and apply it to the right-side points. The final product is two point clouds in which the left side of the curb is fully aligned and overlapping (Figure 3A). If there was any movement between the two dates of acquisition, the two point

clouds on the right side will not overlap and the distances between the point clouds can be estimated using ICP. Any differences in position of the right-side point clouds reflect the displacement of the curb over the corresponding time interval, which we interpret as the local curb offset due to fault creep.

The differences between the two point clouds are measured within CloudCompare, which decomposes the results into three orthogonal directions: curb-vertical (Z), curb-parallel (X), and curb-perpendicular (Y; Figure 3). In our reference frame the curb-perpendicular displacements will be positive (i.e. positive Y-values) for a right-lateral sense of motion. For right-side-up motion, the curb-vertical values will be positive (positive Z-values), and for opening (i.e., curbs moving apart), the curb-parallel values will be positive (positive X-values). For each curb direction, we plot a histogram showing the range of spatial differences between the two point clouds (Figure 3B-D). We estimate a best-fitting Gaussian distribution to each peak of each histogram to obtain the mean and standard deviation of the curb displacement in each direction. These are then divided by the time interval between observations to obtain curb offset rates and uncertainties (Table S3). Finally, we combine the curb-perpendicular and curb-vertical components for a given site into a resultant vector, which we name the Y-Z displacement or offset rate; curb-parallel motion is hard to constrain using our methodology, but our results demonstrate it is a small component of displacement, and so we choose not to include it for the purposes of comparing displacements (see results below).

The nature of curb deformation resulting from underlying fault creep is such that most curbs appear to be displaced at the nearest tooled control joint. In rare cases a new crack forms in the curb's cross-sectional plane and displaces mid-curb. Regardless of the angle between the local curb orientation and the fault strike (and whether displacement occurs on a tooled control joint or new crack), the curb displacements are consistently perpendicular to the curb axis (the curb's cross-sectional plane) in this mechanically favorable orientation. The angle between the local curb orientation and fault strike were used to convert Y-Z curb offset rates to fault-parallel rates (i.e. fault creep rates).

RESULTS

In total, twenty sites in Fremont were measured from 2015 to 2018 spanning three main areas (divided into northern, central, and southern sections; Figure 1, Table S1, S2). For each site, we measured the displacements from the longest time interval available, up to three years, and additional time intervals of interest (Table S3). Where possible, displacement results are considered in the context of 'ensembles' of closely located sites and additional field photos of fault-related damage (see Supplementary Information for more details).

Curb Displacement Rates

The distribution of curb movement varies from site to site with most displacement observed in the curb-perpendicular and curb-vertical directions, and minimal movement observed in the curb-parallel direction (Figure 4). The lack of detectable curb-parallel displacement could in part reflect the difficulty in uniquely matching points in the curb-parallel direction (i.e., there is no physical curb plane to difference in the curb-parallel direction, unlike in the curb-vertical or curb-perpendicular directions), however we do not visually observe significant curb-parallel opening at most of our sites.

Seven of the curbs show the largest displacement in the curb-perpendicular direction (sites 4, 12, 35, 36, 34, 33, 24). Six of the sites show most movement in the curb-vertical direction (sites 3, 2, 14, 11, 10, 21). Seven curb sites show approximately equal amounts of movement in both directions (e.g. sites 1, 5, 6, 17, 18, 23, 22). Site 10 shows a large curb-vertical displacement of −3.85 ± 0.22 mm/yr with respect to the left side of the curb being aligned (relative upward movement of the left-side curb, verified by field observations; Figures S1, S2). Site 12, across the road from site 10, also shows large vertical displacement but the resulting left-side up step in the sidewalk has been shaved down by the city as it poses a tripping hazard (Figure 6).

We plot curb-perpendicular and curb-vertical displacement rates in their along-strike order to understand the spatial movement of each curb (Figure 4). The curb-perpendicular values are projected into the local fault strike directions to determine principal components of fault creep (Figure 5). Site pairs 1-2, 10-11, and 21-23 are on the same side of the same road in each case

and are summed to show the total movement accommodated by a fault transect (Figure 6). Sites 4 and 33 have trees growing in close proximity, which could influence the movement of the curb, and are not considered in the curb interpretations.

From our comparisons of the curb-perpendicular velocities at sites on opposite sides of the same road, we identify areas that show contraction and others that show extension. Sites 17–18 and 35–36 both show contraction, with the northernmost curb exhibiting more curb-perpendicular movement than the southernmost curb (Figures S3–S6). Although site 4 is not considered in our interpretation, field photos at site 5 show contraction observed from tiles buckling between the offset curb site and the pathway. Sites 11–12 and 21–24 both show extension in which the northernmost curb has less curb-perpendicular movement than the southernmost curb (Figures S2, S6). This is corroborated by field photos from 2009 that show pronounced en echelon cracks in the asphalt road pavement that create local depressions (Figure S2).

The curb offset rates are projected into the fault-parallel direction to resolve the amount of fault movement per year necessary to produce these Y-Z offset rates (Table S3). The projected values range from ~0.5 mm/yr to ~4.5 mm/yr – showing wider variation than the rates estimated from the nearest alignment array to the curb site (Figure 7). As we shall discuss below, this may reflect the difference in measurement aperture between our SfM models (~3 m) and alignment arrays (~120 m).

Curb Displacement Variations in Time

We made multiple field visits to our curb sites in Fremont during the study. Not every site yielded a usable point cloud from every visit – on some occasions our target curbs were blocked by cars, obscured by vegetation overgrowth or by repainting (e.g. Figures S7, S8; Table S2). In other cases, we discovered that we had insufficient overlap between our photographs to make a high-quality point cloud, or that we could not identify enough features between a pair of point clouds to perform an alignment. However, for 14 of our sites, we were able to estimate offset

rates from our 2016 and 2018 surveys, spanning a period of 2.42 years (Table S3). Six sites had measurements spanning 2017-2018 (sites 1, 4, 11, 10, 17, 35), three sites spanning 2015–2016 (sites 33, 23, 21) and two sites spanning 2016–2017 (sites 1 and 12). Comparing the other intervals of time to the 2016–2018 timespan, three of the 2017–2018 sites fall within the 2016–2018 fitted line (Figure 8) but the others do not. This could be the result of temporally varying creep rates. One exception is site 23 which shows little to no Y-Z curb offset in our study period, but comparing our models to photos taken in 2009, movement at this specific site may be occurring in the curb-parallel direction (Figures S1, S6).

At a handful of sites (sites 1, 10, 12, and 17) we were able to make more than one successful comparison between point clouds from different years (i.e., 2016–2017, 2017–2018, and/or 2016–2018; Figures 8 and 9). Displacement estimates from each site suggest that the amplitude of curb-perpendicular offset each year is variable. At three out of four of the sites (1, 12 and 17), we infer that the direction of displacement also varies (Figure 9); for example, site 12 shows movement dominated by curb-vertical and then curb-perpendicular displacement in alternating years. We are not aware of similar observations from other creeping faults.

DISCUSSION

Spatio-Temporal Distribution of Deformation on a Creeping Fault

Our estimated fault-parallel curb offset rates along the Hayward Fault in Fremont vary from 0.7 mm/yr to 4.9 mm/yr, and consistently show rates lower than creep rates estimated at nearby alignment arrays (5.2–6.1 mm/yr; McFarland et al., 2016, 2019). We anticipate this discrepancy is due to due to fault deformation occurring over a wider zone than the < 3 m of curb length that we sample at each site; this wider deforming zone is better captured by the wider (~120 m) aperture covered by alignment arrays. Thus, each offset curb likely captures only a fraction of the total creep rate, even if it straddles a mapped fault trace. A similar effect can be seen in creepmeter data (e.g. Bilham et al., 2009), which also measure a smaller aperture (10–30 m) than alignment arrays.

A comparison of estimated deformation rates and their uncertainties (Figure 8) suggests that our small-aperture curb offset rates show more spatiotemporal variability than the wider-aperture alignment array rates. These observations could be explained as properties of fault creep being detected (i.e. the cross-fault distribution of strain due to fault creep changes through time) and/or effects of more localized site conditions (i.e. soil moisture and root activity dynamics). The underlying causes for these observations are beyond the scope of this study but we would encourage additional studies to pursue this in the future.

We consider deformation that occurs within the wider fault zone, but is not expressed as curb offsets, to be distributed (i.e. "off-fault") deformation. We quantify this off-fault deformation as the percentage difference between the alignment array creep rate and the Y-Z curb offset rate projected into the fault direction and plot it in Figure 7. We find that off-fault deformation is pervasive in the Hayward Fault zone in Fremont. There are nine curb sites where > 50% of the deformation is off-fault, six sites that show 20–40% off-fault deformation, and one location where off-fault deformation is negligible. In this latter case, we sum the offset rates from two curb sites (sites 10 and 11) 3.5 m apart, on the same side of the road, suggesting that in some cases, measuring multiple successive offset curbs can capture the full offset rate.

Several complications may exist in determining the significance of an offset curb as equivalent to fault creep rate at depth. Imperfect cohesion between the concrete curb slab, the soil-sedimentary fill beneath, and the bedrock-hosted fault zone could result in a lost transference of creep rate to the built surface. Poor lateral alignment of the tooled control joints between the concrete curb slabs and the fault zone at depth could build resistance to offset and reduce creep rate transmission to the surface. Similarly, we observe a high angle between the fault strike and orientations of slab joints seems to result in a lower apparent creep rate. Though rare, at some sites (e.g. site 11, Figure 6) curb segments exhibit evidence of distributed deformation by bending rather than discrete offset; our method is not sensitive to measuring this non-rigid deformation component. The effects of proximal trees on vertical curb offsets are typically easy to identify in the field (e.g. Figure S9) but possible horizontal rate effects of subsurface roots and pipes in

resisting displacement remain unknown. The narrowness of the fault slip zone and the depth to which the bedrock-hosted fault zone is buried may both be factors in the style and distribution of deformation at the surface (Figure 10). Despite all these considerations, curb-scale offset measurements still provide a minimum fault creep rate, constrain creep rate localization when paired with wider cross-fault techniques, and give valuable constraints on the rate and style of creeping fault deformation in urban environments.

Our repeat observations of individual curbs clearly show inter-annual temporal variability in creep rates consistent with annual alignment array results from 2015-2018 (McFarland et al, 2016, 2019; Figure 8). Similarly, though not temporally overlapping with our observation period, Shirzaei and Bürgmann (2013) inverted 18 years of InSAR-derived surface deformation observations on the Hayward Fault and also found temporal variations in creep rates at specific sites. This invites the questions: Can an along-strike pulse of rate acceleration or deceleration be identified? Do changes in groundwater conditions or local seismicity affect rate? A clear trend is not obvious given our limited spatio-temporal sample size, but this observation further highlights the value of frequently repeated, high density, high accuracy measurements to understand spatio-temporal variation of fault creep and motivates future studies of this type.

Monitoring Creeping Faults

We suggest the ease, efficiency, and accuracy of using SfM photogrammetry to document fault creep rates at the street curb scale (10^{-1} to 10^{1} m) is a valuable complement to other common methods used to observe creep. These include GPS (e.g. Titus et al., 2011), satellite InSAR (e.g. Schmidt et al., 2005, Shirzaei and Bürgmann, 2013), airborne InSAR (e.g. Donnellan et al., 2017), geodolite (e.g. Lisowski & Prescott, 1981), alignment arrays (e.g. Lienkaemper et al. 2014), creepmeters (e.g. Bilham et al., 2009), terrestrial lidar scanning (e.g. Karabacak et al. 2011), and traditional cultural feature measurements (e.g. Lienkaemper & Prescott, 1989). Our SfM approach is arguably the only method in which a minimally trained citizen scientist could collect high resolution field data.

The Width of Creeping Fault Zones

Scott et al. (2020a) recently demonstrated the ability of differential airborne lidar to determine spatially dense three-component deformation measurements along a 150 km section of the creeping central San Andreas and Calaveras faults. They examined subsets of the 11-13 year differenced data in 400 m along-fault intervals and cross-fault widths of 1-2 km, and generally found their right-lateral creep rates to exceed those derived from creepmeter (30 m cross-fault width), alignment array (~150 m cross-fault width), and electric distance measurement survey (2-3 km cross-fault widths) observations. These results highlight the importance of cross-fault width in sampling apparent creep rate due to the width distribution of deformation (i.e. "off-fault" deformation), but also suggest some methods are better suited to capture maximum rates. Wide cross-fault aperture methods are valuable in capturing the maximum rate of fault creep, while narrow cross-fault aperture methods, like our SfM curb approach, are most instructive in determining spatio-temporal variability at a scale that will affect the built environment. An intermediate scale method yet to be tested on creeping faults would be to use a camera-equipped low-flying drone at a street scale for repeat SfM or optical pixel correlation (e.g. Milliner et al., 2021), which could help to quantify the localization of fault deformation occurring near the fault trace versus within the larger zone of deformation measured by other methods.

CONCLUSIONS

Repeat observations of offset curbs through a constellation of consumer-grade photographs allows for the determination of three-component fault creep rates using structure-from-motion photogrammetry and topographic differencing of resultant point clouds. Field data collection is easy and efficient such that a site could be surveyed in minutes by a non-expert citizen scientist, and yet can yield high-precision results. The narrow cross-fault width of observation (10^{-1} to 10^{1} m) complements wider cross-fault observation methods like creepmeters and alignment arrays and is most directly applicable to understanding the influence of fault creep on deforming a built

environment. At twenty-one sites on the Hayward Fault in Fremont, CA we observed right-lateral creep rates up to 4.9 mm/yr and found that on average individual offset curbs record <40% of the overall creep rate measured from nearby alignment arrays (which span a fault-perpendicular distance of ~120 m).

ACKNOWLEDGMENTS

DATA AVAILABILITY

The data underlying this article are available in a Zenodo repository, at https://doi.org/10.5281/zenodo.6426482.
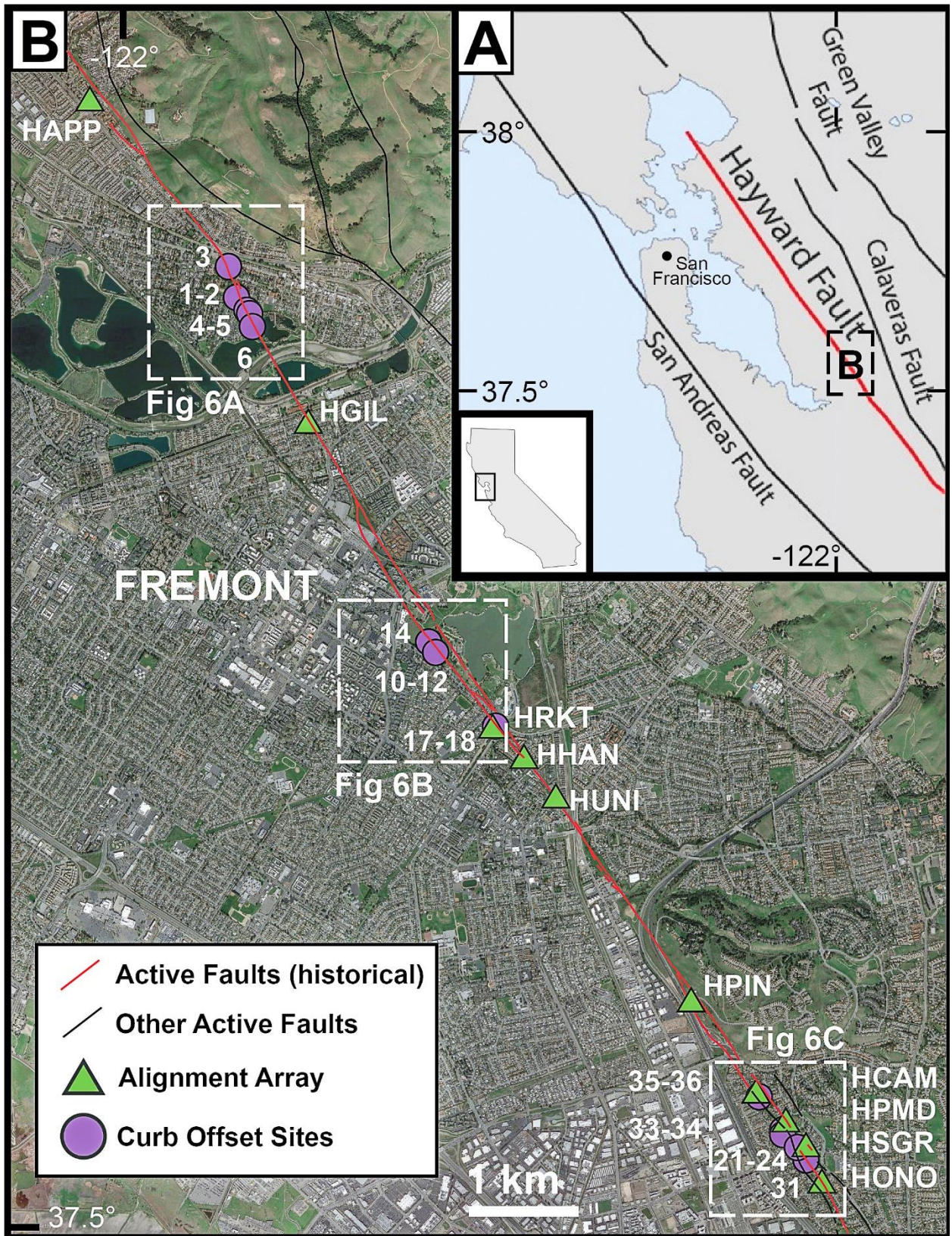
Figure 1. (A) Location of the Hayward Fault in northern California. (B) Map of Hayward Fault traces (Lienkaemper, 2009), the distribution of alignment arrays (McFarland et al., 2016), and the locations of monitored offset curbs in Fremont, CA (this study). Dashed boxes show areas of the offset curbs shown in Figure 5.
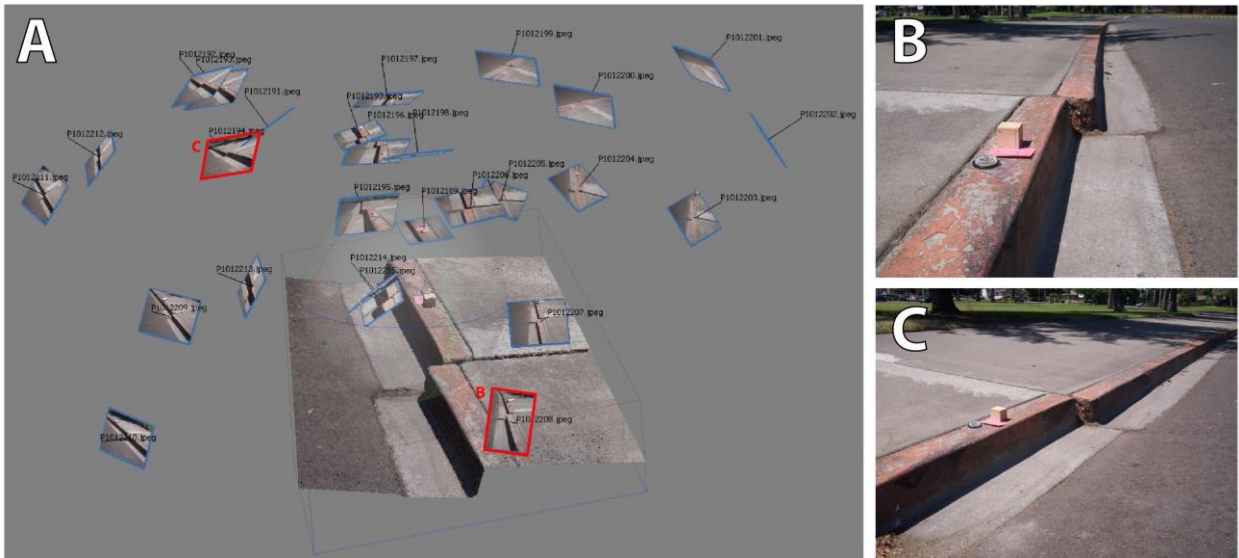
Figure 2. Typical structure-from-motion (SfM) survey setup. (A) An example view of offset curb site 12 in Agisoft Metashape software showing 27 inward looking photo positions and orientations (blue rectangles with black normals) and the resultant 3D point cloud determined using SfM photogrammetry techniques. Notice the wide array of photo positions and vantage points focused on the curb. The two pictures in the red boxes show the orientation of the two pictures in B and C. In each panel notice the precision crafted wooden scale cube, 5 cm on a side.
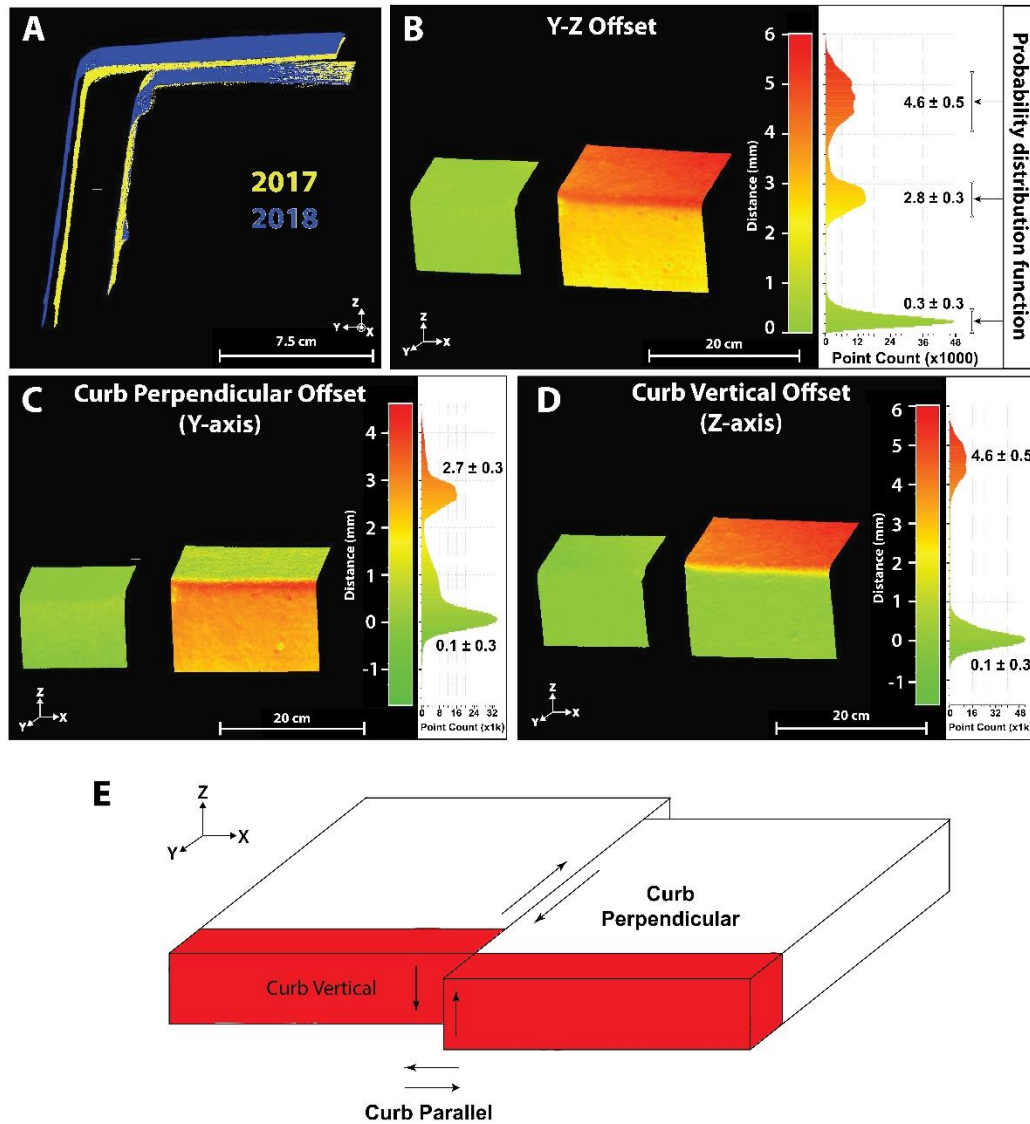
Figure 3. (A) 3D model distance difference for site 4, spanning 2017 to 2018, showing the aligned point clouds viewed in the curb-parallel direction and that the 2018 point cloud (blue) moved up and towards the street compared to the 2017 point cloud (yellow). (B) Resultant Y-Z curb offset. On the left side (green) the two point clouds are aligned and the right side moved in the Y- and Z- directions. The Y-Z curb offset is decomposed into the curb-vertical (Z-axis) movement (C) and curb-perpendicular (Y-axis) movement (D). The curb-perpendicular movement (C) shows the right side moved a positive distance of ~2.5 mm (red/orange), the curb-vertical (D) movement shows the right side moved a positive distance, upward, a total of ~4.5 mm (red). Notice the histograms at the right of the color scales in panels B, C, and D, that indicate the probability distribution function for each offset estimate. The high curb-vertical rate at this site is in part due to tree influence (see Supplementary Information for more details). (E) Local curb reference system utilized in this study. Directions of X, Y, and Z axes denote positive directions.
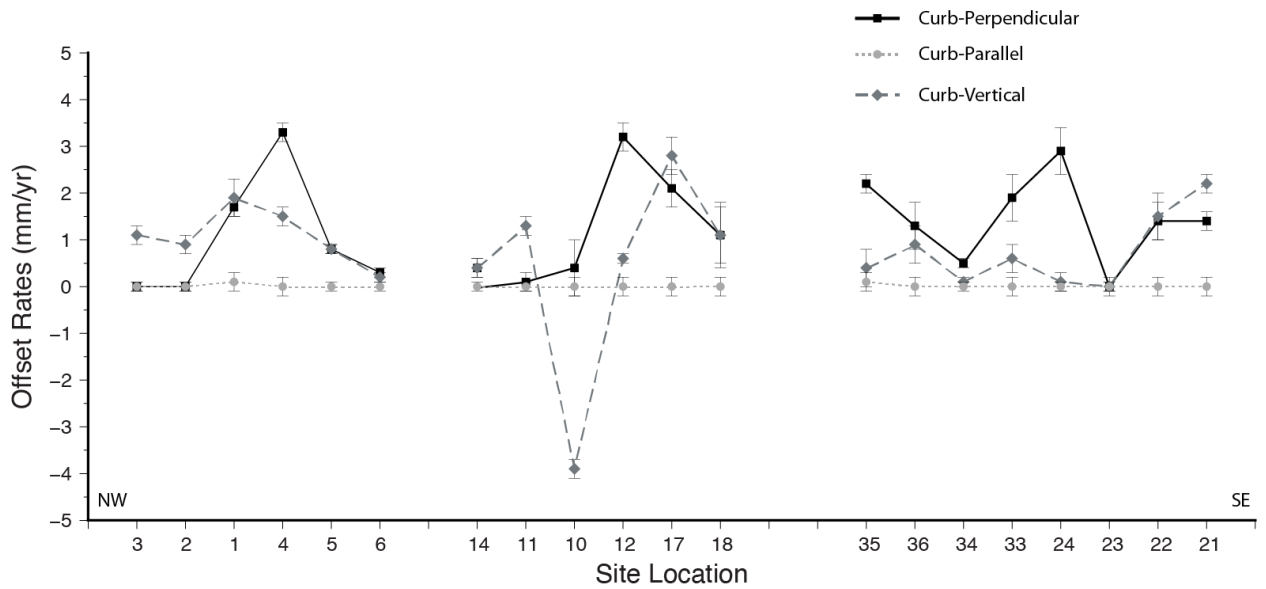
Figure 4. Offset rates for each site in the curb-perpendicular (strike-slip; square, solid line), curb-vertical (dip-slip; diamond, dark gray dashed line), and curb-parallel (extensional; circle, light gray dotted line) directions using the longest time interval available. The rates are with respect to the aligned left side of the offset curb. The uncertainties are calculated from the one standard deviation displacement measurement, divided by the time interval for each offset curb. The horizontal axis shows the position of each site in their along-strike order and is not to scale.
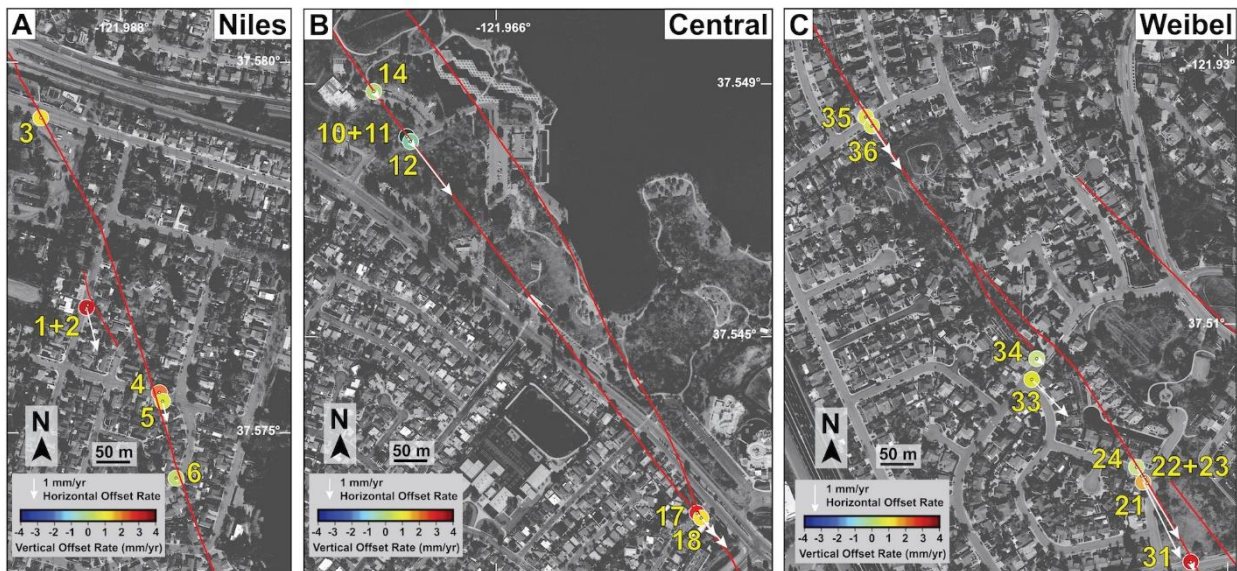

Figure 5. Mapped fault traces (red lines; Lienkaemper, 2009), curb-perpendicular values projected into the local fault strike direction (white arrows), and curb-vertical (colored circles) offset rates of each offset curb. A, B, and C are noted as insets in Figure 1 as the northern, middle, and southern sections of sites. Sites that are on the same side of the road are summed together (i.e., sites 1–2, sites 10–11, sites 21–23).
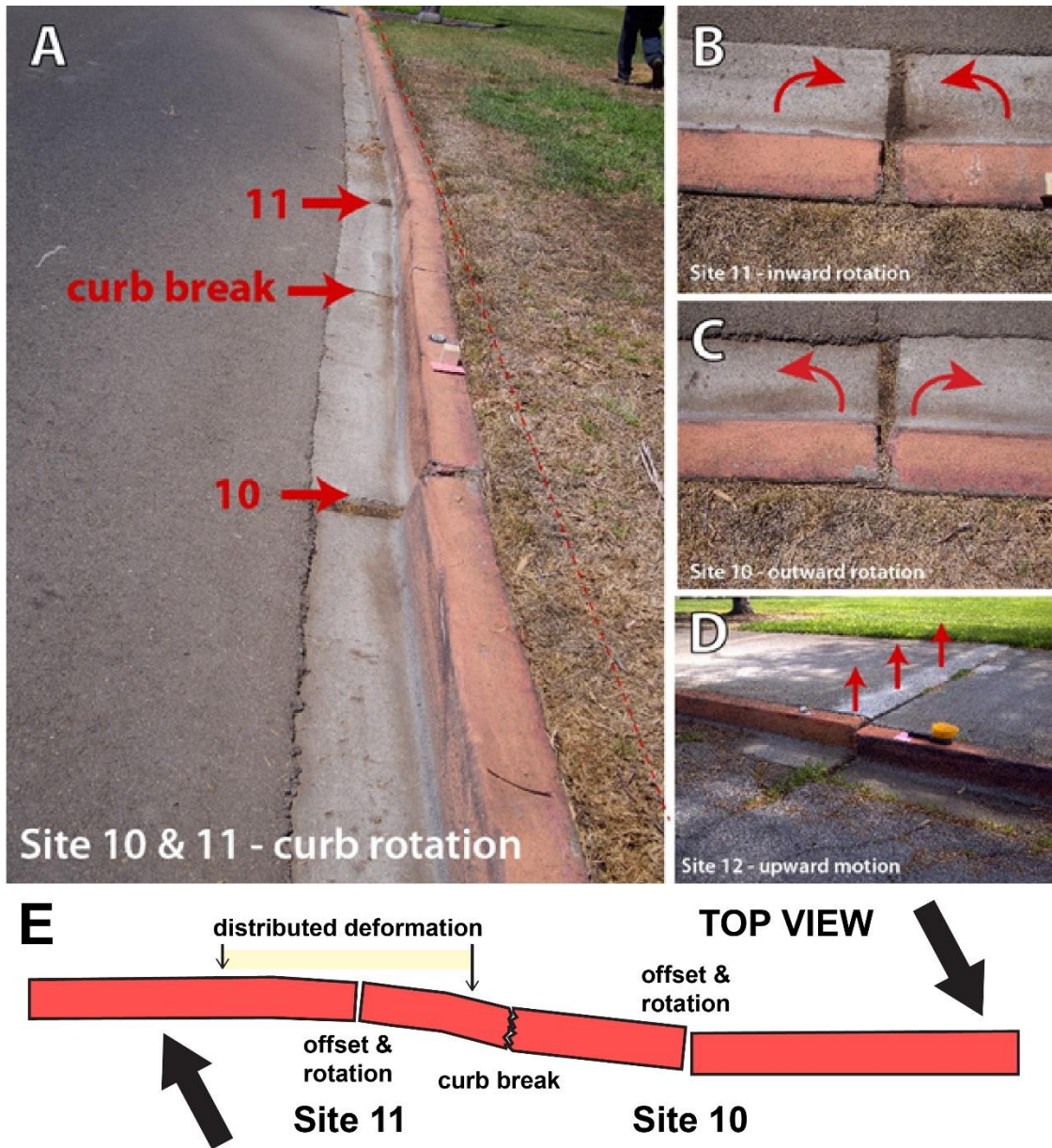
Figure 6. Evidence of fault creep beyond a single curb offset. (A) View looking along curb at sites 10 and 11 that are summed to determine creep rate. Notice the evidence of distributed deformation (bending of curb panel) near Site 11 that is not accounted for in our measurements. Notice also the break in the curb panel between sites 10 and 11. (B & C) Top view photos showing rotation of curb panels consistent with a dextral shear sense. (D) Site 12 (opposite side of street as 10 and 11) where enough vertical offset occurred to require the curb edge to be ground to minimize the tripping hazard. (E) Top view schematic of sites 10 and 11 highlighting key characteristics of deformation due to fault creep (curb panel offset and rotation, brittle breaking of curb panel, distributed deformation across about 2m. Height of curb is ~12 cm.
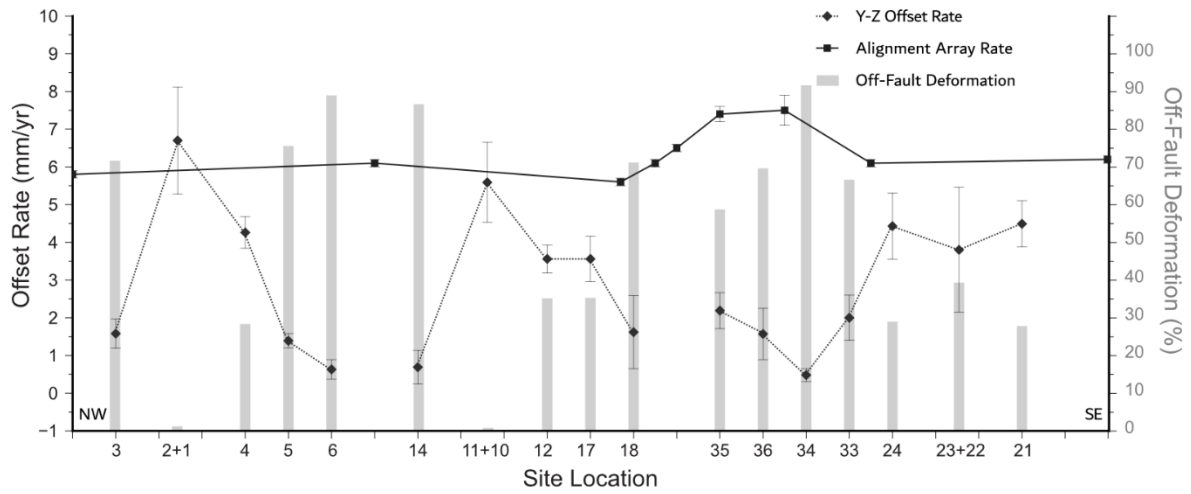
Figure 7. Y-Z curb offset rates (curb-perpendicular and curb-vertical resultant offset rates projected into the fault direction (diamonds) compared to alignment array rates (squares). Note that the curb offset rates are generally less than the alignment array rates with uncertainty. Sites that are on the same side of the road are summed together. Off-fault deformation (right axis; light gray bars) is offset that appears to occur wider than the curb-scale Y-Z offset and assumes that the nearest alignment array captures the full rate. Thus off-fault deformation is equal to 100% minus the Y-Z curb rate percentage of the nearest alignment array rate. Sites located the same side of the road are summed together (i.e., 2 and 1, 10 and 11, and 22 and 23). The horizontal axis shows the position of each site in their along-strike order and is not to scale. The lines joining successive points are to help visualize the connections of the type of measurements and are not meant to imply that the displacements vary linearly between.
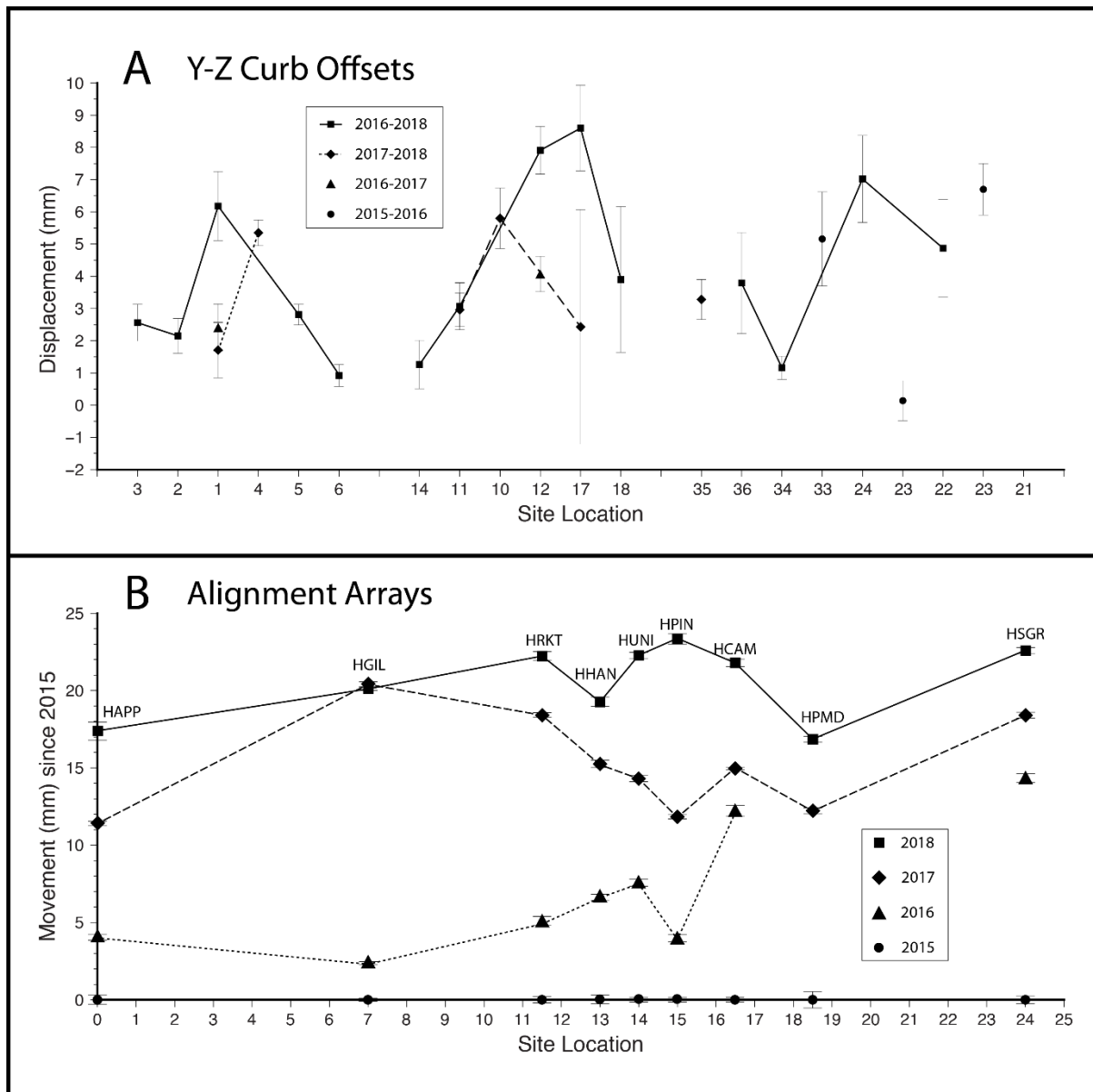
Figure 8. Spatio-temporal variations in creep displacement. (A) Comparisons of Y-Z displacements (i.e. the length of the resultant vector from the curb-perpendicular and curb-vertical components) for each time interval measured (2016–2018, 2017–2018, 2016–2017, 2015–2018). Site 23 shows negligible movement likely due to being on the same side of the road as site 22. (B) Variations in yearly alignment array cumulative fault-parallel displacement measurements in Fremont, CA starting from 2015 (data from McFarland et al., 2016, 2019). The lines joining successive points are to illustrate the connections of the measurements in time and are not meant to imply that the displacements vary linearly between alignment arrays. Neighboring curb sites are shown for reference. The amount of displacement between each successive year at any given site is not consistent suggesting that some years the fault moves more than others, corroborated by our curb offset measurements.
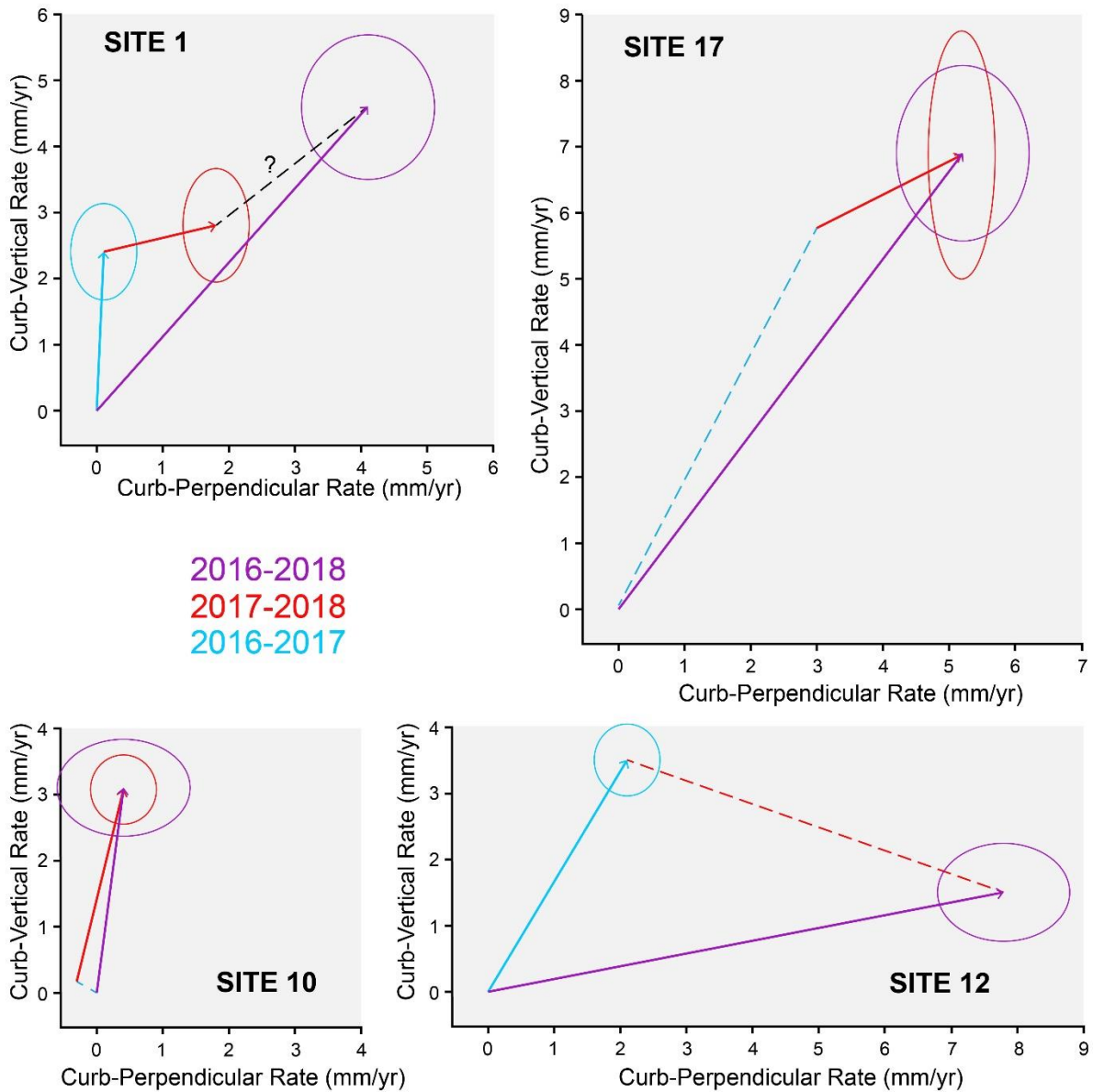
Figure 9. Curb displacement vectors for sites 1, 10, 12, and 17 showing the temporal and kinematic variability in movement for three observation periods (2016-2017, 2017-2018, 2016-2018) with error ellipses. The intervals between surveys are not precisely one year in duration, but each site was surveyed on the same day in the given year. Dashed lines highlight presumed motion during an interval lacking a survey. We infer variability in the amount of displacement each year at all four sites. Site 10 shows similar displacements in the period 2016-2018 as are estimated for 2017-2018, suggesting that the majority of the displacement occurred in the latter period. Sites 1, 17 and 12 additionally show changes in the direction of displacement, manifest as different vector directions in each period. The obliquity of the fault trace with respect to the orientation of the curb may account for some of the displacement imbalance at Site 1.
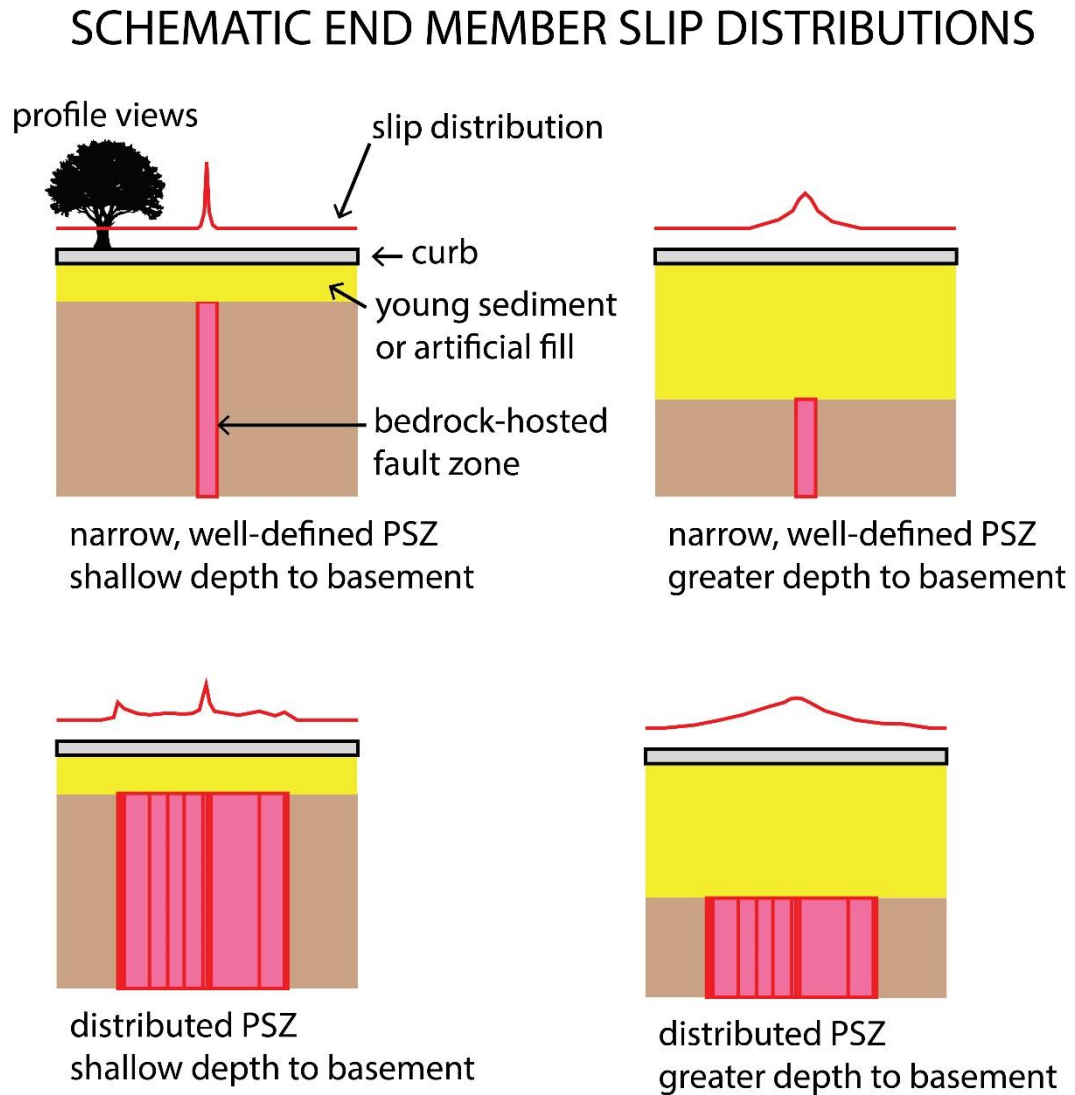
SCHEMATIC END MEMBER SLIP DISTRIBUTIONS

Figure 10. Conceptual models illustrating expected surface slip distributions manifest by principal slip zone (PSZ) width and complexity, and the depth to which the bedrock-hosted fault zone is buried.

REFERENCES

Bemis, S. P., Micklethwaite, S., Turner, D., James, M. R., Akciz, S., Thiele, S. T., & Bangash, H. A., 2014. Ground-based and uav-based photogrammetry: A multi-scale, high-resolution mapping tool for structural geology and paleoseismology, *Journal of Structural Geology*, 69, 163–178.

Bilham, R., Suszek, N., & Pinkney, S., 2009. California Creepmeters, *Seismological Research Letters*, 75(4), 481–492.

Burgmann, R., Schmidt, D. A., Nadeau, R. M., D'Alessio, M. A., Fielding, E. J., Manaker, D., McEvilly, T. V., & Murray, M. H., 2000. Earthquake Potential Along the Northern Hayward Fault, California, *Science*, 289(August), 1178–1183.

Chen, Y. & Medioni, G., 1992. Object modelling by registration of multiple range images, *Image and vision computing*, 10(3), 145–155.

Donnellan, A., Arrowsmith, R., & DeLong, S., 2017. Spatio-Temporal Mapping of Plate Boundary Faults in California Using Geodetic Imaging, Geosciences, 7, 15, doi:10.3390/geosciences7010015

Doolin, D. M., Wells, D. L., & Williams, P. L., 2005. Assessment of fault-creep deformation at memorial stadium, University of California, Berkeley, California, *Environmental & Engineering Geoscience*, 11(2), 125–139.

Fonstad, M. A., Dietrich, J. T., Courville, B. C., Jensen, J. L., & Carbonneau, P.E., 2013. Topographic structure from motion: A new development in photogrammetric measurement: Earth Surface Processes and Landforms , v. 38, p. 421–430, doi:10.1002/esp.3366.

Funning, G. J., Blueford, J. R., York, K., & McAlpine, G., 2010. 'Citizen Creepmeters': involving high school students in monitoring of fault movements using inexpensive equipment. In AGU *Fall Meeting Abstracts, Vol 2010, pp. ED14A-06.*

Johnson, K., Nissen, E., Saripalli, S., Arrowsmith, J. R., McGarey, P., Scharer, K., Williams, P., & Blisniuk, K., 2014. Rapid mapping of ultrafine fault zone topography with structure from motion, *Geosphere*, 10(5), 969–986.

James, M. R. and Robson, S., 2012. Straightforward reconstruction of 3D surfaces and topography with a camera: Accuracy and geoscience application: Journal of Geophysical Research , 117, F03017, doi:10.1029/2011JF002289

Karabacak, V., Altunel, E. & Cakir, Z., 2011, Monitoring aseismic surface creep along the North Anatolian Fault (Turkey) using ground-based LIDAR, Earth and Planetary Science Letters, 304(1–2), 64-70, https://doi.org/10.1016/j.epsl.2011.01.017.

Lienkaemper, J., 2009. Digital database of recently active traces along the Hayward Fault, California: US Geological Survey Data Series DS-177, 20 p.

Lienkaemper, J. J., 1992. Map of recently active traces of the Hayward Fault, Alameda and Contra Costa counties, California.

Lienkaemper, J. J. & Galehouse, J. S., 1998. New evidence doubles the seismic potential of the Hayward Fault, *Seismological Research Letters*, 69(6), 519–523.

Lienkaemper, J. J. & Williams, P. L., 2007. A record of large earthquakes on the southern Hayward Fault for the past 1800 years, *Bulletin of the Seismological Society of America*, 97(6), 1803–1819.

Lienkaemper, J. J., Williams, P. L., & Guilderson, T. P., 2010. Evidence for a twelfth large earthquake on the southern Hayward Fault in the past 1900 years, *Bulletin of the Seismological Society of America*, 100(5A), 2024–2034.

Lienkaemper, J. J., McFarland, F. S., Simpson, R. W., & Caskey, S. J., 2014. Using Surface Creep Rate to Infer Fraction Locked for Sections of the San Andreas Fault System in Northern California from Alignment Array and GPS Data SE, *Bulletin of the Seismological Society of America*, 104(6), 3094–3114.

Lin, R.-G., 2016. The 'Holy Grail' for earthquake scientists has been accidentally destroyed. Los Angeles Times, https://www.latimes.com/local/lanow/la-me-ln-earthquake-curb-destroyed-20160705-snap-htmlstory.html , retrieved 2021/07/15

Lisowski, M. and Prescott, W. H., 1981. Short-range distance measurements along the San Andreas fault system in central California, 1975 to 1979. Bulletin of the Seismological Society of America 1981; 71 (5): 1607–1624. doi: https://doi.org/10.1785/BSSA0710051607

Lowe, D. G., 1999. Object recognition from local scale-invariant features, Proceedings of the Seventh IEEE International Conference on Computer Vision, 1999, pp. 1150-1157 vol.2, doi: 10.1109/ICCV.1999.790410.

McFarland, F.S., Lienkaemper, J.J., and Caskey, S.J., 2016, Data from theodolite measurements of creep rates on San Francisco Bay Region faults, California (ver. 1.8, March 2016): U.S. Geological Survey Open-File Report 2009-1119, 21 p. and data files, http://pubs.usgs.gov/of/2009/1119/.

McFarland, F.S., Lienkaemper, J.J., and Caskey, S.J., 2019. Data from Theodolite Measurements of creep rates on San Francisco Bay Region faults, California (version 1.2, March 2019): U.S. Geological Survey data release, https://doi.org/10.5066/F76W9896.

Milliner, C., Donnellan, A., Aati, S., Avouac, J.-P., Zinke, R., Dolan, J.F., Wang, K., and Burgmann, R., 2021. Bookshelf Kinematics and the Effect of Dilation on Fault Zone Inelastic Deformation: Examples From Optical Image Correlation Measurement, of the 2019 Ridgecrest Earth Sequence, *Journal of Geophysical Research: Solid Earth*, 126(3).

Nissen, E., Krishnan, A. K., Arrowsmith, J. R., & Saripalli, S., 2012. Three-dimensional surface displacements and rotations from differencing pre-and post-earthquake lidar point clouds, *Geophysical Research Letters*, 39(16).

Nissen, E., Maruyama, T., Arrowsmith, J. R., Elliott, J. R., Krishnan, A. K., Oskin, M. E., & Saripalli, S., 2014. Coseismic fault zone deformation revealed with differential lidar: Examples from Japanese Mw~ 7 intraplate earthquakes. Earth and Planetary Science Letters, 405, 244-256.

Radbruch, D. H. & Lennert, B. J., 1966. Damage to culvert under Memorial Stadium, University of California, Berkeley, caused by slippage in the Hayward Fault zone, *Bulletin of the Seismological Society of America*, 56(2), 295–304.

Schmidt, D. A., Burgmann, R., Nadeau, R. M., & D'Alessio, M., 2005. Distribution of aseismic slip rate on the Hayward fault inferred from seismic and geodetic data, *Journal of Geophysical Research B: Solid Earth*, 110(8), 1–15.

Scott, C. P., DeLong, S. B., & Arrowsmith, J. R., 2020a. Distribution of aseismic deformation along the Central San Andreas and Calaveras faults from differencing repeat airborne lidar. Geophysical Research Letters, 47, e2020GL090628.https://doi.org/10.1029/2020GL090628

Scott, C., Bunds, M., Shirzaei, M., & Toke, N. 2020b. Creep along the central San Andreas Fault from surface fractures, topographic differencing, and InSAR. Journal of Geophysical Research: Solid Earth, 125(10), e2020JB019762. https://doi.org/ 10.1029/2020JB019762.

Shirzaei, M. and R. Bürgmann, 2013. Time-dependent model of creep on the Hayward Fault from joint inversion of 18 years of InSAR and surface creep data, J. Geophys. Res-Solid Earth, 118, 1733–1746, doi:10.1002/jgrb.50149

Stoffer, P. W., 2008. Where's the Hayward Fault? A Green Guide to the Fault, *Geological Survey Open-File Report*, 2008-1135, 1 – 96.

Teza, G., A. Galgaro, N. Zaltron, and R. Genevois (2007), Terrestrial laser scanner to detect landslide displacement fields: A new approach, Int. J. Remote Sens., 28(16), 3425–3446. https://doi.org/10.1080/01431160601024234

Titus, S.J., Dyson, M., DeMets, C., Tikoff, B., Rolandone, R., and Burgmann, R., 2011. Geologic versus geodetic deformation adjacent to the San Andreas fault, central California: Geological Society of America Bulletin, v. 123, p. 794-820; doi:10.1130/B30150.1

Trexler, C. C., Morelan, A. E., Oskin, M. E., & Kreylos, O., 2018. Surface slip from the 2014 South Napa earthquake measured with structure from motion and 3-D virtual reality. Geophysical Research Letters, 45, 5985– 5991. https://doi.org/10.1029/2018GL078012

Westoby, M. J., Brasington, J., Glasser, N. F., Hambrey, M. J., & Reynolds, J., 2012. 'Structure-from-Motion' photogrammetry: A low-cost, effective tool for geoscience applications, *Geomorphology*, 179, 300–314.

Yu, E. & Segall, P., 1996. Slip in the 1868 Hayward earthquake from the analysis of historical triangulation data, *Journal of Geophysical Research: Solid Earth*, 101(B7), 16101–16118.